RESEARCH ARTICLE | SEPTEMBER 08 2025

Luminescence properties of GeSn laser materials: Influence of buffered substrates

Martin Aagaard ; Omar Concepción ; Dan Buca ; Zoran Ikonic ; Brian Julsgaard

J. Appl. Phys. 138, 105701 (2025)
https://doi.org/10.1063/5.0281958

Journal of Applied Physics ARTICLE pubs.aip.org/aip/jap

Luminescence properties of GeSn laser materials: Influence of buffered substrates

Cite as: J. Appl. Phys. **138**, 105701 (2025); doi: 10.1063/5.0281958
Submitted: 22 May 2025 · Accepted: 7 August 2025 ·
Published Online: 8 September 2025

Martin Aagaard,[1,a)] Omar Concepción,[2] Dan Buca,[2] Zoran Ikonic,[3] and Brian Julsgaard[1]

AFFILIATIONS

[1]Department of Physics and Astronomy, Aarhus University, Ny Munkegade 120, 8000 Aarhus C, Denmark
[2]Institute of Semiconductor Nanoelectronics, Peter Grünberg Institute 9 (PGI 9) and JARA-Fundamentals of Future Information Technologies, Forschungszentrum Jülich, 52428 Jülich, Germany
[3]Pollard Institute, School of Electronic and Electrical Engineering, University of Leeds, Leeds LS2 9JT, United Kingdom

[a)]**Author to whom correspondence should be addressed:** aagaard@phys.au.dk

ABSTRACT

Time-resolved photoluminescence spectroscopy is used to measure the luminescence lifetime of two direct bandgap GeSn samples. The GeSn samples are similar in respect to the material properties, except for one being grown on a thin Ge-post-deposition annealed buffered layer, while the other is grown on a thick Ge virtual substrate. The total photoluminescence intensity and the lifetime of the samples are compared as a function of temperature between 20 and 300 K and pump fluence between 2.5×10^{13} and 1×10^{15} cm^{-2}, showing little difference between the two samples. The luminescence lifetime varies only little with temperature, and calculations of the total photoluminescence intensity based on k·p theory are compared to experimentally attained values, yielding a good functional agreement vs temperature. The results point to the L-valley as one of the primary inhibiting factors of the photoluminescence intensity at non-cryogenic temperatures.

I. INTRODUCTION

The development of laser materials based on GeSn alloys has come a long way since it was first suggested by Goodman in 1982.[1] Initially, interest in this material was limited, but interest has increased within the last 15 years, much of this being due to the development in growth techniques, which made GeSn viable for use in photonic devices.[2–5] GeSn, more precisely written as $Ge_{1-x}Sn_x$, draws this attention because of its direct bandgap at Sn contents above 10 at. %—but generally this number depends on the strain of the alloy.[6] The direct bandgap is a unique property among the group-IV materials, and thus, the luminescence of GeSn provides a keystone for developing group-IV photonics. Given this, it would come as no surprise that a focus of research during the past 15 years has been GeSn lasers. In 2015, the first GeSn laser emission was demonstrated,[7] and in 2022, the first optically pumped GeSn laser operating at room temperature was demonstrated.[8] The first electrically injected GeSn laser operating at 100 K was demonstrated in 2020.[9] Such a laser would open the door for a Si-integrated light source that is monolithically grown,[5] and developing an electrically injected laser working at room temperature is a focus point for the field. The 100 K limit has recently been pushed further to 140 K,[10] but this still leaves a challenge to overcome before reaching room temperature operation.

An important part in reaching room temperature operation is to further the understanding of what limits the efficiency of the laser material beyond cryogenic temperatures. A main limiting factor is the short lifetime of excited carriers in GeSn. However, the topic of recombination quickly becomes a muddy one as different Sn contents, film thickness, growth techniques, and substrates all could play a role. Therefore, measured lifetimes span over a wide range from 0.05 to 1.5 ns.[4] This entire span of lifetimes is quite short compared to, e.g., InAsSbBi, which like GeSn has a luminescence peak in the midinfrared range (around 4.0 μm) and a lifetime in the range of 100 ns.[11,12] It is, therefore, clear that to push for better GeSn lasers, a deeper understanding of the parameters affecting the lifetime of GeSn is needed.

This study focuses on how the choice of a buffer layer impacts the lifetime of GeSn. This is done by comparing the lifetimes of two GeSn samples that have a GeSn layer that is similar in Sn

content, strain, and film thickness. The only difference is that, in one sample, the GeSn layer is grown on a thick germanium-virtual substrate (GeVS) buffer layer, and in the other sample, the GeSn layer is grown on a thin post-deposition-annealed germanium buffer layer (GePDA); both have an underlying silicon substrate. Experience shows that GeSn/GePDA is not suitable for device manufacturing—for this, a GeVS buffer is preferable. This opens the question whether the luminescence characteristics of the top GeSn film will differ for the two studied cases. We find that there are no major differences in the luminescence lifetime between the two samples across a wide temperature range. Furthermore, both calculations, based on 8-band k·p theory, and experimental data show a similar behavior of the total photoluminescence (PL) intensity as a function of temperature. This agreement points to the population of the L-valley and not activation of defects as being the main limiting factor of the PL intensity at non-cryogenic temperatures.

II. METHODS

This section first presents the experimental methods—mainly time-resolved photoluminescence spectroscopy. Second, k·p theory is briefly presented along with the essential equations for calculating PL spectra.

A. Experimental methods

The two GeSn samples that are investigated here were grown in an industry-compatible reduced-pressure chemical vapor deposition reactor.[13] The GeVS substrate, which was grown following the method described in Ref. 14, is 2.5 μm thick and ensures that the GeSn is grown on a substrate that is smooth, relaxed, and with an estimated threading dislocation density (TDD) of $\sim 10^6$ cm^{-2}. The GePDA substrate of the other sample is 0.42 μm thick and with an estimated TDD in the range of $10^7 - 5 \times 10^7$ cm^{-2}. This sample would typically be deemed too poor for device manufacturing but is widely used for material characterization.[15–18] We shall from now on just call the GeSn sample on the GeVS: "GeVS" and similarly the GeSn sample on the GePDA substrate: "PDA."

The material parameters are presented in Table I. The Sn contents and film thicknesses were extracted by fitting the random spectra of Rutherford back-scattering spectrometry (RBS). The strain parameters were determined by x-ray diffraction reciprocal space maps (XRD-RSM), which are provided in Sec. III of the supplementary material.

Time-resolved photoluminescence spectroscopy (TRPLS) is used to measure the photoluminescence of the GeSn samples. An overview of the experimental setup is presented in Fig. 1. The

TABLE I. Material parameters of the two samples. x is the Sn content, $\varepsilon_{\parallel}$ is the in-plane strain, $\varepsilon_{\perp}$ is the out-of-plane strain, R is the degree of strain relaxation, d_{film} is the thickness of the GeSn film, and d_{buff} is the thickness of the buffer layer.

Sample	$x(at.\%)$	$\varepsilon_{\parallel}(\%)$	$\varepsilon_{\perp}(\%)$	R (%)	$d_{\text{film}}(nm)$	$d_{\text{buff}}(nm)$
PDA	12.5	-0.31	0.25	82	495	420
GeVS	11.5	-0.29	0.22	81	440	2500

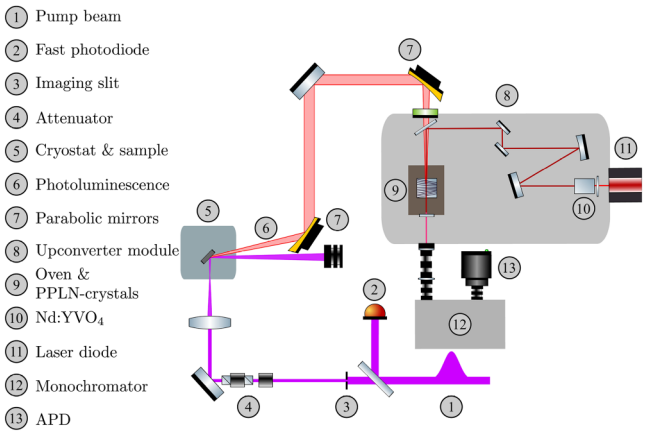

FIG. 1. Overview of the TRPLS setup. The pump beam is imaged onto the sample. The photoluminescence of the excited sample is collected and collimated by a parabolic mirror and focused by a second parabolic mirror onto the stack of fanned PPLN crystals where the upconversion happens. The upconverted signal is then passed through a monochromator and onto an APD. The time difference between the start signal from the fast photodiode and the stop signal from the APD provides the time resolution.

sample is excited using a 800 nm Ti:sapphire femtosecond laser with a pulse width of less than 100 fs—which we shall call the pump laser. Before hitting the sample, a fraction of the pump laser is split off with a beam splitter, which hits a fast photodiode (TDA 200 from PicoQuant), and the signal from this fast photodiode gives the start signal for the measurement. The rest of the pump laser passes through an imaging slit and an attenuator—consisting of a $\frac{\lambda}{2}$-plate and a Glan–Taylor polarizer—before being imaged onto the sample with a beam size of 0.84 mm^2 and a flat-top beam profile. The sample is placed in a cryostat that enables cooling of the sample down to 20 K. After being excited by the pump laser, the sample emits light that is collected and collimated by a parabolic mirror, and a second parabolic mirror further focuses it into the upconverter module (specifications given in Ref. 19), which uses three-wave mixing in a periodically poled lithium niobate (PPLN) crystal to make the infrared PL detectable by silicon-based detectors. On the entrance hole of the upconverter module, a Ge window is placed to allow only infrared wavelengths entering the upconverter module, and on the exit hole, a 950 nm short-pass filter and a 600 nm long-pass filter allow for the transmission of only the upconverted signal. After the upconverter module, the upconverted signal is further spectrally filtered by a monochromator (McPherson model 218) and finally detected by an avalanche photodiode (APD) (MPD-100-CTB from PicoQuant). By adjusting slits on the monochromator, it is ensured that the PL is attenuated sufficiently for single photon counting to work. The signal from the APD is the stop signal of the measurement and the time differences between the start and stop signals are logged using a time-correlating electronics board (TimeHarp 260 from PicoQuant).

The upconversion efficiency depends on the setting of the upconverter module, and a relative calibration of this is necessary to determine the PL spectrum. The calibration is made by

measuring the signal of a globar (Hawkeye IR-Si207) at different upconversion wavelengths and assuming that the globar radiates with a spectrum compatible with blackbody radiation. The temperature of the globar is determined by measuring the spectrum of the globar using a spectrometer with a range of 940–1664 nm and fitting a blackbody radiation spectrum to this. Also using the globar, the percentage of transmitted light as a function of the monochromator slit setting is calibrated. The calibration of especially the upconversion efficiency does fluctuate within a day of measurements, meaning that the measurements of the PL spectrum are associated with some uncertainty estimated to be around 20%, but since the PL intensity spans orders of magnitude, this is not consequential for the conclusions of this work.

The short carrier lifetime of GeSn requires that the instrument response function (IRF) of the measurement apparatus is taken into account as its temporal width will typically be of a similar size. Hence, the data need to be regarded as a convolution between the IRF and the true PL signal, and in turn, the IRF must be measured to enable proper data analysis. The IRF is measured as the TRPLS signal acquired by upconverting femtosecond laser pulses at a wavelength of 2.4 μm delivered by a TOPAS. Note it was checked that the setting of the upconverter did not have a major impact on the IRF, which is, therefore, common for all photon energies. The FWHM of the IRF is measured to be 71 ps.

B. Numerical methods

The numerical methods are based on k·p theory, and the 8-band k·p theory has long been the method of choice for calculations of the GeSn band structure around the Γ-point and, in turn, calculations of carrier concentrations, PL spectra, and modelling of GeSn bulk and quantum well lasers.[6,7,16,20–23] The 8-band k·p theory is suitable for GeSn since most of the luminescence-related processes involve states near the Γ-point. Most of the calculations found in the literature are based on Bahder's papers[24,25] on a 8-band k·p Hamiltonian for strained zinc-blende crystals. One should note that the 8-band k·p model not only accounts for the interaction of Bahder's eight basis states but also includes distant bands perturbatively. When applied to crystals with diamond structure like Ge and Sn, the inversion parameter is set to zero.[24] However, a weak point in 8-band k·p theory is that it does not describe the L-valley. Since the difference between the direct and indirect bandgaps, i.e., the directness, of GeSn is small, the L-valley in the conduction band cannot be ignored. Therefore, it is usually included using the effective-mass model,[6,16,20] which is a good approximation because the high density-of-states (DOS) and the fourfold degeneracy of the L-valley imply that electrons occupy only the states near the L-valley minima where the effective mass approximation works well.

For the calculation presented here, we use 8-band k·p theory combined with the effective mass model for the L-valley conduction band. Most of the parameters for the k·p Hamiltonian are given in Ref. 6, except the Luttinger parameters and the spin–orbit split-off energy that are from Ref. 26. Furthermore, to avoid spurious solutions, the method from Ref. 27 is used. Note that there is a difference in sign between the definitions of a_v of Ref. 6 and a of Ref. 25. This can be seen from the definition itself but also by considering a hydrostatic strain that in Ref. 6 leads to an average valence-band shift of $\Delta E_{\mathrm{v,av}} = a_v(e_{xx} + e_{yy} + e_{zz})$, where e_{ii} is the ii'th-strain matrix element. Considering the same case in the Hamiltonian in Ref. 25 gives $\Delta E_{\mathrm{v,av}} = -a(e_{xx} + e_{yy} + e_{zz})$, illustrating the sign difference.

With the calculated band structure of the Γ-valley and the L-valley, the density of states in the appropriate range of energies can then be calculated from the expression[28]

$$\mathrm{DOS}(E) = \frac{1}{V}\sum_{\mathrm{c,v}}\sum_{\mathbf{k}}\delta_{E(\mathbf{k}),E} = \frac{1}{(2\pi)^3}\sum_{\mathrm{c,v}}\int \mathrm{d}\,\mathbf{k}\delta(E(\mathbf{k}) - E). \quad (1)$$

Here, V is the quantization volume meaning that Eq. (1) represents the density of states per volume. Equation (1) contains delta functions that can be difficult to treat numerically, and tetrahedron integration has been used to make the integration of the δ-function on a $\mathbf{k}$-grid.[29,30] The calculated DOS is then used to find the Fermi-energy of the system in equilibrium and the quasi-Fermi energies in quasi-equilibrium for any given electron and hole density. Note that the summation, $\sum_{\mathrm{c,v}}$, in Eq. (1) includes the two conduction bands and six valence bands from the 8-band k·p theory around the Γ-point as well as the L-valley conduction band.

This work is focused on the temperature-dependent luminescence rate. The luminescence rate is the number of photons emitted per unit time per unit volume per unit energy, which is further summed over the different polarizations of the emitted photons, since no polarization dependence has been observed in our experiments. The expression[16]

$$R_{\mathrm{sp}}(\hbar\omega) = \frac{e^2\mathrm{Re}\{n\}\omega}{3m^2\hbar\pi\varepsilon_0 c^3}\frac{1}{(2\pi)^3}\sum_{\mathrm{c,v},\hat{\boldsymbol{\varepsilon}}}\int \mathrm{d}\,\mathbf{k}\,|\hat{\boldsymbol{\varepsilon}}\cdot\langle \mathrm{c}|\,\mathbf{p}|\mathrm{v}\rangle|^2 \times \delta(E_{\mathrm{c}}(\mathbf{k}) - E_{\mathrm{v}}(\mathbf{k}) - \hbar\omega)f_{\mathrm{e}}(E(\mathbf{k}))f_{\mathrm{h}}(E(\mathbf{k})) \quad (2)$$

is used, where ω, n, f_{e}, f_{h}, $\mathbf{p}$, and $\hat{\boldsymbol{\varepsilon}}$ are the photon angular frequency, complex refractive index, electron Fermi–Dirac distribution, hole Fermi–Dirac distribution, momentum operator, and polarization unit vector, respectively. E_{c} and E_{v} are the conduction and valence band energies, respectively, both dependent on $\mathbf{k}$. These are calculated by the k·p method, which provides the respective conduction band and valence band wavefunctions, $|\mathrm{c}\rangle$ and $|\mathrm{v}\rangle$. The summation, $\sum_{\mathrm{c,v}}$, in Eq. (2) includes the two conduction bands and six valence bands from the 8-band k·p theory. Also, Eqs. (2) and (1) do not include a factor of 2 to account for spin because the k·p calculations provide spin-degenerate bands, so the sum over conduction bands and valence bands accounts for it.

III. RESULTS AND DISCUSSION

In this section, the luminescence properties of the GeVS sample and the PDA sample are described and compared through a series of TRPLS curves such as those shown in Fig. 2. These are acquired for different pump fluences, Φ_{pump}, and different temperatures, T. The series of curves shown in Fig. 2 are acquired at $T = 20$ K and for two different photon energies, i.e., 0.54 and

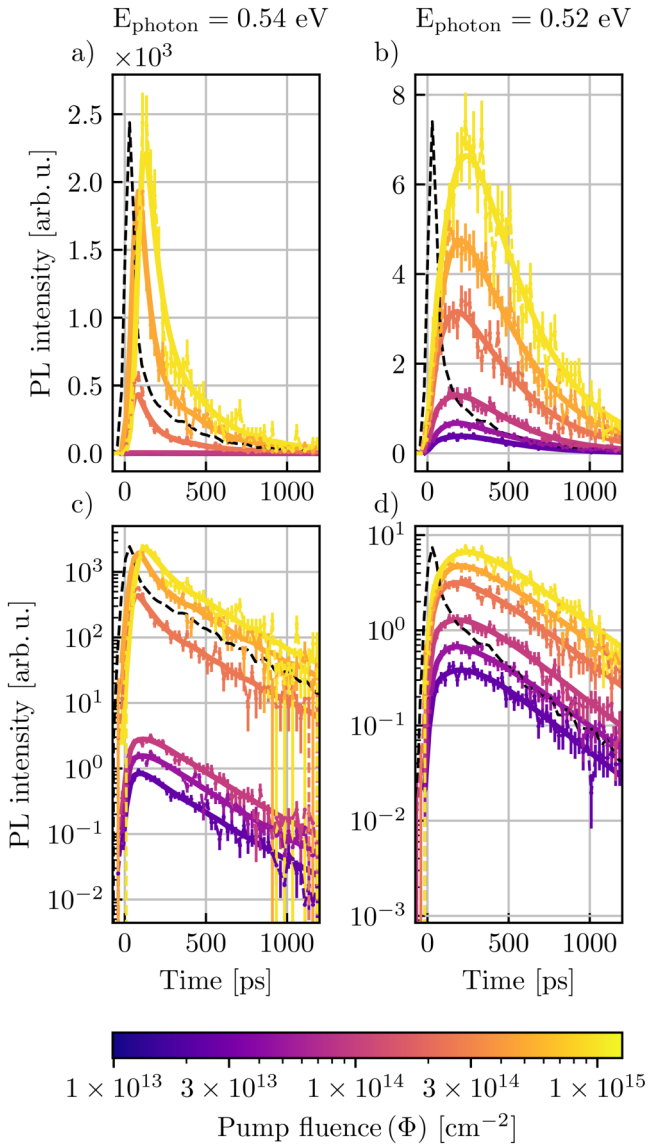

FIG. 2. TRPLS data for the GeVS sample taken at 20 K at two different photon energies along with the fits using Eq. (4). Note panels (a) and (c) [(b) and (d)] present the same data but on a linear and a log scale, respectively. The black dashed line is the IRF, which for long times determinates the shape of the TRPLS signal as seen clearly in panel (c).

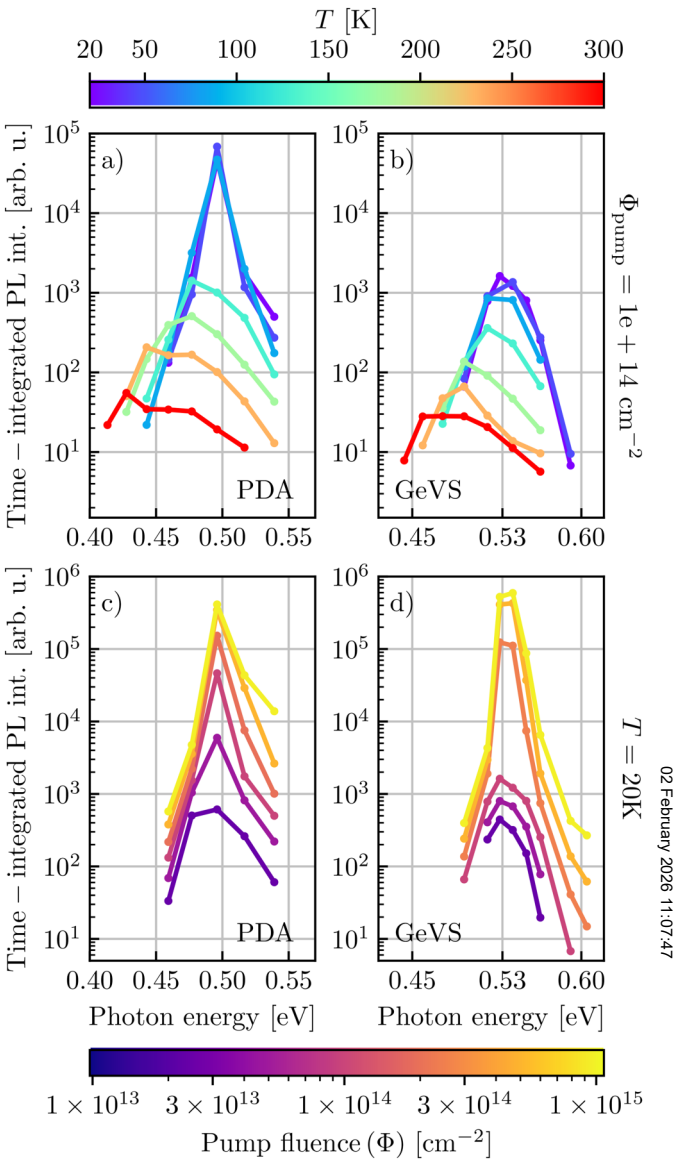

FIG. 3. In panels (a) and (b), the spectra of the time-integrated PL intensity for PDA and GeVS, respectively, are shown for a constant $\Phi_{pump} = 1 \times 10^{14}$ cm^{-2}. Panels (c) and (d) show the spectra of the time-integrated PL intensity for a constant temperature $T = 20$ K.

0.52 eV. Looking at Figs. 2(a) and 2(c)—which are the same data but different y-scales—it is clear that the PL intensity is highly dependent on the pump fluence, and high excitation powers can cause the signal to sharply increase—a feature that we attribute to amplified spontaneous emission (ASE).[31] By comparing Figs. 2(a) and 2(c) to 2(b) and 2(d), it is clear that this effect is also very dependent on the photon energy. This feature is further demonstrated in Fig. 3, where in panels a and b, the time-integrated PL intensities for the PDA and GeVS, respectively, are shown for a constant fluence, i.e., varying temperature, and in panels c and d, again, respectively, for PDA and GeVS, the time-integrated PL intensities are shown for a constant T, i.e., varying fluence. Figures 3(a) and 3(b) show a redshift of the PL as is expected from the reduction in the bandgap predicted by the Varshni equation.[6] Also, a general broadening is seen adhering to the temperature broadening of the Fermi–Dirac distribution. For the PDA sample, in

particular, it is clear that for temperatures above 100 K, there is a sudden drop. This is attributed to ASE, no longer being effective. For temperatures below 100 K, ASE is very dominant, so much that the PDA sample has a much greater light emission than the GeVS. A similar sudden drop in time-integrated PL intensity is also seen in Fig. 3(d), where the GeVS at $T = 20$ K has a fluence-threshold for ASE at $\Phi_{pump} = 1 \times 10^{14}\,cm^{-2}$. Here, it is also clear that ASE occurs for a narrow range of photon energies, thus the dramatic difference between the Φ_{pump} dependencies in Fig. 2. The two interfaces of air/GeSn and GeVS (or PDA)/Si constitute a planar waveguide in which ASE can occur. As seen in Table I, the waveguide is 2940 nm thick with 440 nm of active layer for the GeVS sample. In comparison, the waveguide of the PDA sample is only 915 nm thick but with 495 nm of active layer. With this in mind, it is no surprise that the PDA sample shows a lower threshold for ASE than the GeVS sample. Since ASE is a consequence of the size of the buffered layer more than an intrinsic GeSn property, emphasis shall be on the fluences that are not dominated by ASE.

Let us now focus on the time dynamics of the TRPLS curves. From Fig. 2, it is seen that the PL intensity can have a rise time, which depends on Φ_{pump} as well as photon energy. Also, the peak of the curve can be very narrow as seen in Fig. 2(a) or very broad as seen in Fig. 2(b). These features of the curves cannot be modeled by a simple exponential model, so to address this, an empirical model,

$$f_{model}(t) = A\frac{e^{-\frac{t}{\tau}}}{1 + e^{-\frac{t-t_{0,delay}}{\tau_{delay}}}}, \tag{3}$$

is employed.[18] No physical significance should in principle be attributed to τ, τ_{delay}, and $t_{0,delay}$; though in the limit of $\tau_{delay} \to 0$, Eq. (3) goes to a single exponential function. Regarding the rise time, it is difficult to pinpoint that physical process might contribute as there is generally a relaxation mechanism that would contribute in both **r**- and **k**-space. One clue to what could cause the rise time is the fact that high photon energies do not have a rise time, and this points to electron-lattice thermalization playing a central role. However, the relatively long rise time of up to 200 ps would fit poorly with the usual thermalization times of a few ps usually stated for Ge.[32,33]

As briefly mentioned in Sec. II A, the IRF has a temporal width comparable to the TRPLS curves, so, to fit the curves, f_{model} is convolved with the IRF, i.e.,

$$f_{fit}(t) = \int_0^\infty \mathrm{IRF}(t - t')f_{model}(t')\mathrm{d}t'. \tag{4}$$

As seen in Fig. 2, this method of fitting is quite robust and works for the different shapes of the TRPLS curves.

Each TRPLS curve is fitted to Eq. (4), and from this, the photon-energy-integrated PL intensity as a function of time can be calculated by numerically integrating over the curves acquired at different photon energies, i.e., $\int f_{model}(t, \hbar\omega)\mathrm{d}\hbar\omega$. The photon-energy-integrated PL intensity then, in turn, allows for calculations of the luminescence lifetime of the GeSn samples by the expression

$$\langle t \rangle = \frac{\int_0^\infty t \int f_{model}(t, \hbar\omega)\mathrm{d}\hbar\omega\mathrm{d}t}{\int_0^\infty \int f_{model}(t, \hbar\omega)\mathrm{d}\hbar\omega\mathrm{d}t}. \tag{5}$$

It should be noted that for $f_{model}(t, \hbar\omega) \to e^{-\frac{t}{\tau}}$, the expression yields $\langle t \rangle = \tau$. Hence, it is the case that when f_{model} takes a physically interpretable form, $\langle t \rangle$ assumes the expected value.

The previously mentioned rise time of the TRPLS curves will affect the value of $\langle t \rangle$ such that an increase in the rise time will cause an increase in $\langle t \rangle$. This is not the best way to determine the material quality, as thermalization effects tend to be much more complex than the decay from a thermalized state. To filter out the contribution of the rise times, one can alternatively calculate

$$\langle t \rangle_{offset} = \frac{\int_{t_{max}}^\infty (t - t_{max}) \int f_{model}(t, \hbar\omega)\mathrm{d}\hbar\omega\mathrm{d}t}{\int_{t_{max}}^\infty \int f_{model}(t, \hbar\omega)\mathrm{d}\hbar\omega\mathrm{d}t}. \tag{6}$$

By choosing t_{max} to be the time by which all the individual TRPLS curves included in the total luminescence have started decaying, $\langle t \rangle_{offset}$ represents the luminescence decay time from a thermalized state.

For each temperature and for fluences that are not affected by ASE, both $\langle t \rangle$ and $\langle t \rangle_{offset}$ are calculated, and a mean over the included fluences is calculated, which is presented in Fig. 4. Looking initially at Fig. 4, it is clear that both samples have surprisingly similar lifetimes both when considering the magnitudes of the lifetimes but also how they depend on the temperature. Focusing on Fig. 4(b), both samples show a slight decrease in the lifetimes until around 100 K where the times plateau or increase as is the case for the PDA sample. This increase is quite counter-intuitive as it is generally hypothesized that defects in GeSn will activate at non-cryogenic temperatures,[34–36] which in turn—all things being equal—would lead to a more effective recombination process and a shorter lifetime. Looking at Fig. 4, there is little that would indicate this.

A different aspect of the luminescence properties is the total PL intensity, i.e., the PL intensity integrated over both time and photon energies, which is shown for the two samples as a function of temperature and for different fluences in Fig. 5. This is presented in an Arrhenius-style plot, which is typically used to enhance the intuition of processes with different characteristic activation energies. Also plotted in Fig. 5 are temperature-dependent total PL curves calculated by k·p theory. These are calculated using a simplistic model for the charge carriers of a single-exponential decay and a homogeneous initial distribution. The band structure of GeSn is calculated using values for the Sn content and the strain that are in between the values of the two samples, i.e., $x_{calc} = 12\%$, $\varepsilon_{\parallel,calc} = -0.3\%$, and $\varepsilon_{\perp,calc} = 0.235\%$. The excitation densities are calculated by the equation $\Delta N = (1 - R)\frac{\Phi_{pump}}{d_{film}}$, assuming $d_{film} = 470\,nm$, a value in-between the film-thicknesses of the samples, and a reflectivity of $R = 0.56$ determined from ellipsometry measurements. These parameters mean that $\Phi_{pump} = 1 \times 10^{14}\,cm^{-2}$ corresponds to $\Delta N = 9.4 \times 10^{17}\,cm^{-3}$. The lifetime of the exponential decay is chosen to be $\tau_{calc} = 110$ ps for all temperatures. This is chosen to match the weakly varying

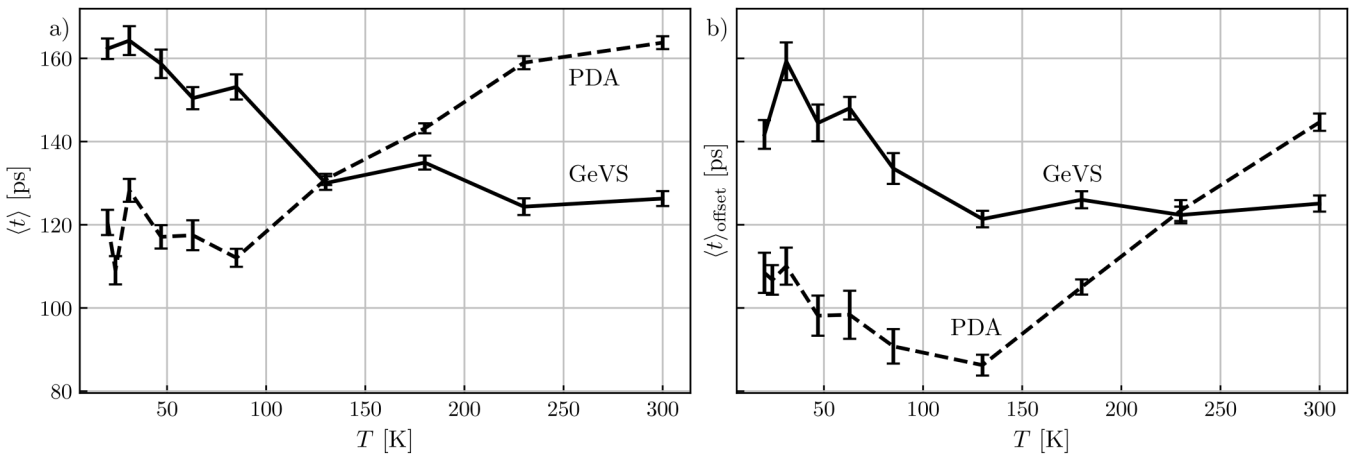

FIG. 4. Mean lifetimes presented as $\langle t \rangle$ in panel (a) and $\langle t \rangle_{\text{offset}}$ in panel (b).

values of $\langle t \rangle_{\text{offset}}$ found in Fig. 4. Finally, a p-doping concentration of 5×10^{17} cm^{-3} is assumed. The PL is then calculated as a function of time by the methods introduced in Sec. II B using the charge carrier densities at each time step assigned by the exponential decay. An underlying limitation of this calculation is the fact that the measured spectra and the theoretically calculated spectra are not in perfect agreement; the calculations predict a broader spectrum than found experimentally. This is investigated a bit further in Sec. I of the supplementary material. We also wish to mention that excitonic effects have been neglected in Eq. (2). Such effects have previously been calculated in the effective-mass approximation for Ge and GeSn luminescence,[37,38] and using these methods in our case shows that we underestimate the luminescence intensity by approximately 50%. However, the temperature variation in this deviation is within the experimental error margins, rendering excitonic effects unnecessary for modeling the temperature variation in our data.

The results of the theoretical calculations are presented with dashed lines in Fig. 5, and here, it is clear that there actually is very good agreement between the trend of the experimental curves and the calculated curves. Both show almost no temperature dependence until around 100 K, where the signal starts to decay rapidly. Note that this modeling does not include any activation of defects; in fact, the high explanatory power indicates that such defects are not needed to explain the decrease in the total PL intensity at higher temperatures found in the experimental results. Rather, the

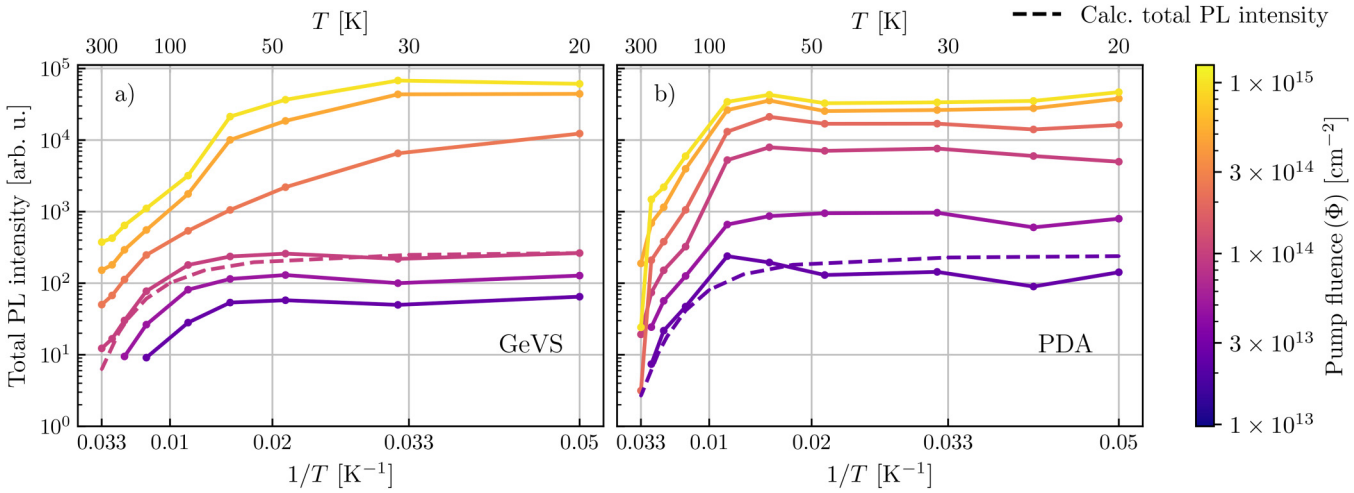

FIG. 5. Panels (a) and (b) show the total PL intensity for GeVS and PDA, respectively, presented on an Arrhenius type plot at different Φ_{pump} together with the k·p theory-based calculations of the total PL intensity normalized to the maximum experimental value.

explanation for the decrease in the total PL intensity is simply the low directness of the direct band of GeSn and the high density of states of the L-valley compared to the Γ-valley, such that at higher temperatures an increasing percentage of carriers are in the L-valley where they recombine non-radiatively. For example, at excitation densities of $\Delta n = 1 \times 10^{17}\,\mathrm{cm}^{-3}$, 0% of the electrons is in the L-valley for 20 K, while for 300 K, 88% of the carriers are in the L-valley. How this changes as a function of electron density and temperature is expanded on in Sec. II of the supplementary material. The population of electrons escaping to the L-valley, influencing the temperature dependence of the PL intensity, is a characteristic of direct-bandgap GeSn alloys, as demonstrated by several research groups.[7,21,39,40] This emphasizes the role that the low directness—along with the short decay time—plays in the future of GeSn lasers.[4,20,41,42]

Returning to the comparison of the TRPLS of the two samples, there is not a huge difference, neither for the PL intensity nor for the lifetimes. Though, in Fig. 5, it would in fact seem that the PDA sample has a more efficient emission of PL at least for intermediate values of Φ_{pump}; however, as previously mentioned, this is associated with a lower threshold for ASE. However, looking at the lower fluences where none of the samples have indications of ASE, the samples show similar performances. The similarity of the samples is interesting, as experience with device manufacturing indicates that a PDA buffer does not give high enough quality GeSn samples, with GeVS being an example of a buffered substrate resulting in a good quality GeSn layer. However, the results show that the two GeSn layers can be grown to equal quality on PDA and GeVS with respect to the luminescence characteristics, which may be explained as follows; both GeSn films have a thickness much larger than the critical thickness, and hence, they both show a large degree of strain relaxation. Misfit dislocations occur upon plastic relaxation when the critical thickness is reached, but the GeSn layer grown further from this point can be of high quality.[7,43] This is consistent with a previous study, where GeSn layers (all grown on GeVS and with similar parameters apart from the layer thickness) showed limited variation in luminescence properties as long as the layer thickness exceeded ∼200 nm and thereby led to a high degree of strain relaxation.[16]

IV. CONCLUSION

In this work, photoluminescence lifetimes and intensities were acquired experimentally using time-resolved photoluminescence spectroscopy. This was measured on two different GeSn samples for temperatures spanning 20–300 K and fluences between 2.5×10^{13} and $1 \times 10^{15}\,\mathrm{cm}^{-2}$. The samples are similar in terms of their GeSn layer, but the substrates that the GeSn layers are grown on vary. One is grown on a 0.42 μm Ge-post-deposition annealed buffered layer while the other is grown on a 2.5 μm Ge virtual substrate. The difference in the substrate of the two samples only slightly affects the luminescence lifetime, and the total photoluminescence intensity is comparable in strength. Furthermore, the photoluminescence intensity as a function of temperature was calculated using k·p theory. These calculations showed good agreement with the experimental data and point to the large percentages of electrons situated in the L-valley as the main inhibitor of the PL intensity at increasing temperatures. This matches well with the measured lifetimes that are almost independent of temperature, thus indicating that no extra defect-related decay channels become activated with increasing temperature as this would be clearly seen in the lifetimes.

SUPPLEMENTARY MATERIAL

See the supplementary material for further discussion on the agreement between the theoretically calculated and experimentally acquired time-integrated photoluminescence spectra, the populations of the Γ-valley and the L-valley as a function of temperature and excitation density, and XRD-RSM data for the two samples.

ACKNOWLEDGMENTS

We thank John Lundsgaard Hansen for assistance with ellipsometry measurements. This work was supported by the Novo Nordisk Foundation (No. NNF20OC0064101), the German Research Foundation (No. 299480227), and the European Commission (No. 101070208).

AUTHOR DECLARATIONS

Conflict of Interest

The authors have no conflicts to disclose.

Author Contributions

Martin Aagaard: Conceptualization (equal); Investigation (lead); Visualization (equal); Writing – original draft (lead); Writing – review & editing (lead). **Omar Concepción:** Resources (lead); Writing – review & editing (equal). **Dan Buca:** Funding acquisition (lead); Resources (supporting). **Zoran Ikonic:** Supervision (supporting); Writing – review & editing (equal). **Brian Julsgaard:** Conceptualization (equal); Funding acquisition (lead); Supervision (lead); Writing – review & editing (equal).

DATA AVAILABILITY

The data that support the findings of this study are available from the corresponding author upon reasonable request.

REFERENCES

[1] C. Goodman, "Direct-gap group IV semiconductors based on tin," IEE Proc. I. Solid State Electron. Dev. UK **129**, 189 (1982).
[2] G. He and H. A. Atwater, "Synthesis of epitaxial Sn_xGe_{1-x} alloy films by ion-assisted molecular beam epitaxy," Nucl. Instrum. Methods Phys. Res. B: Beam Interact. Mater. At. **106**, 126–132 (1995).
[3] J. Taraci, S. Zollner, M. R. McCartney, J. Menendez, M. A. Santana-Aranda, D. J. Smith, A. Haaland, A. V. Tutukin, G. Gundersen, G. Wolf, and J. Kouvetakis, "Synthesis of silicon-based infrared semiconductors in the Ge-Sn system using molecular chemistry methods," J. Am. Chem. Soc. **123**, 10980–10987 (2001).
[4] A. Giunto and A. Fontcuberta i Morral, "Defects in Ge and GeSn and their impact on optoelectronic properties," Appl. Phys. Rev. **11**, 041333 (2024).
[5] O. Moutanabbir, S. Assali, X. Gong, E. O'Reilly, C. A. Broderick, B. Marzban, J. Witzens, W. Du, S.-Q. Yu, A. Chelnokov, D. Buca, and D. Nam, "Monolithic infrared silicon photonics: The rise of (Si)GeSn semiconductors," Appl. Phys. Lett. **118**, 110502 (2021).

[6]D. Rainko, Z. Ikonic, N. Vukmirović, D. Stange, N. von den Driesch, D. Grützmacher, and D. Buca, "Investigation of carrier confinement in direct bandgap GeSn/SiGeSn 2D and 0D heterostructures," Sci. Rep. **8**, 15557 (2018).
[7]S. Wirths, R. Geiger, N. von den Driesch, G. Mussler, T. Stoica, S. Mantl, Z. Ikonic, M. Luysberg, S. Chiussi, J. M. Hartmann, H. Sigg, J. Faist, D. Buca, and D. Grützmacher, "Lasing in direct-bandgap GeSn alloy grown on Si," Nat. Photonics **9**, 88–92 (2015).
[8]J. Chrétien, Q. M. Thai, M. Frauenrath, L. Casiez, A. Chelnokov, V. Reboud, J. M. Hartmann, M. El Kurdi, N. Pauc, and V. Calvo, "Room temperature optically pumped GeSn microdisk lasers," Appl. Phys. Lett. **120**, 051107 (2022).
[9]Y. Zhou, Y. Miao, S. Ojo, H. Tran, G. Abernathy, J. M. Grant, S. Amoah, G. Salamo, W. Du, J. Liu, J. Margetis, J. Tolle, Y. hang Zhang, G. Sun, R. A. Soref, B. Li, and S.-Q. Yu, "Electrically injected GeSn lasers on Si operating up to 100 K," Optica **7**, 924–928 (2020).
[10]S. Acharya, H. Stanchu, R. Kumar, S. Ojo, M. Alher, M. Benamara, G.-E. Chang, B. Li, W. Du, and S.-Q. Yu, "Electrically injected mid-infrared GeSn laser on Si operating at 140 K," IEEE J. Sel. Top. Quant. **31**, 1–7 (2025).
[11]P. Petluru, P. C. Grant, A. J. Muhowski, I. M. Obermeier, M. S. Milosavljevic, S. R. Johnson, D. Wasserman, E. H. Steenbergen, and P. T. Webster, "Minority carrier lifetime and photoluminescence of mid-wave infrared InAsSbBi," Appl. Phys. Lett. **117**, 061103 (2020).
[12]F. A. Estévez H, M. Bergthold, O. Maksimov, H. B. Bhandari, C. P. Morath, A. W. Duchane, P. T. Webster, and D. Wasserman, "Enhanced minority carrier lifetime in bulk hydrogen-passivated InAsSbBi," Appl. Phys. Lett. **124**, 021104 (2024).
[13]O. Concepción, N. B. Søgaard, J.-H. Bae, Y. Yamamoto, A. T. Tiedemann, Z. Ikonic, G. Capellini, Q.-T. Zhao, D. Grützmacher, and D. Buca, "Isothermal heteroepitaxy of $Ge_{1-x}Sn_x$ structures for electronic and photonic applications," ACS Appl. Energy Mater. **5**, 2268–2275 (2023).
[14]J. Hartmann and T. Marion, "Impact of flows, temperature and pressure on the GeSn growth kinetics with a digermane and tin tetrachloride chemistry," Mater. Sci. Semicond. Process. **169**, 107893 (2024).
[15]O. Concepción, J. Tiscareño-Ramirez, A. A. Chimienti, T. Classen, A. A. Corley-Wiciak, A. Tomadin, D. Spirito, D. Pisignano, P. Graziosi, Z. Ikonic, Q. T. Zhao, D. Grützmacher, G. Capellini, S. Roddaro, M. Virgilio, and D. Buca, "Room temperature lattice thermal conductivity of GeSn alloys," ACS Appl. Energy Mater. **7**, 4394–4401 (2024).
[16]D. Stange, S. Wirths, N. von den Driesch, G. Mussler, T. Stoica, Z. Ikonic, J.-M. Hartmann, S. Mantl, D. Grützmacher, and D. Buca, "Optical transitions in direct-bandgap Ge_{1-x} Sn_x alloys," ACS Photonics **2**, 1539–1545 (2015).
[17]P. Kaul, O. Concepción, D. H. Wielens, P. Zellekens, C. Li, Z. Ikonic, K. Ishibashi, Q.-T. Zhao, A. Brinkman, D. Grützmacher, and D. Buca, "Phase-coherent transport in GeSn alloys on Si," Adv. Electron. Mater. **11**, 2400565 (2025).
[18]B. Julsgaard, N. Von Den Driesch, P. Tidemand-Lichtenberg, C. Pedersen, Z. Ikonic, and D. Buca, "Carrier lifetime of GeSn measured by spectrally resolved picosecond photoluminescence spectroscopy," Photonics Res. **8**, 788 (2020).
[19]P. Tidemand-Lichtenberg, M. Aagaard, A. S. Ashik, C. Pedersen, and B. Julsgaard, "Tunable infrared upconversion module for the 1.9 to 5.5 μm range," Opt. Lett. **47**, 6189–6192 (2022).
[20]A. Ellis, D. Duffy, I. Marko, S. Acharya, W. Du, S. Q. Yu, and S. Sweeney, "Challenges for room temperature operation of electrically pumped GeSn lasers," Sci. Rep. **14**, 10318 (2024).
[21]S. Assali, A. Dijkstra, A. Attiaoui, E. Bouthillier, J. Haverkort, and O. Moutanabbir, "Midinfrared emission and absorption in strained and relaxed direct-band-gap $Ge_{1-x}Sn_x$ semiconductors," Phys. Rev. Appl. **15**, 024031 (2021).
[22]B. Marzban, D. Stange, D. Rainko, Z. Ikonic, D. Buca, and J. Witzens, "Modeling of a SiGeSn quantum well laser," Photonics Res. **9**, 1234–1254 (2021).
[23]G. Daligou, A. Attiaoui, S. Assali, P. Del Vecchio, and O. Moutanabbir, "Radiative carrier lifetime in $Ge_{1-x}Sn_x$ midinfrared emitters," Phys. Rev. Appl. **20**, 064001 (2023).
[24]T. B. Bahder, "Eight-band k·p model of strained zinc-blende crystals," Phys. Rev. B **41**, 11992–12001 (1990).
[25]T. B. Bahder, "Erratum: Eight-band k·p model of strained zinc-blende crystals [Phys. Rev. B 41, 11 992 (1990)]," Phys. Rev. B **46**, 9913 (1992).
[26]S.-Q. Liu and S.-T. Yen, "Extraction of eight-band k·p parameters from empirical pseudopotentials for GeSn," J. Appl. Phys. **125**, 245701 (2019).
[27]B. A. Foreman, "Elimination of spurious solutions from eight-band k·p theory," Phys. Rev. B **56**, R12748–R12751 (1997).
[28]G. Grosso and G. P. Parravicini, *Solid State Physics*, 2nd ed. (Elsevier Science & Technology, Chantilly, 2013).
[29]G. Gilat and N. R. Bharatiya, "Tetrahedron method of zone integration: Inclusion of matrix elements," Phys. Rev. B **12**, 3479–3481 (1975).
[30]P. Lambin and J. P. Vigneron, "Computation of crystal Green's functions in the complex-energy plane with the use of the analytical tetrahedron method," Phys. Rev. B **29**, 3430–3437 (1984).
[31]P. W. Milonni and J. H. Eberly, *Lasers* (John Wiley & Sons, New York, 1988).
[32]G. Mak and H. M. Van Driel, "Femtosecond transmission spectroscopy at the direct band edge of germanium," Phys. Rev. B **49**, 16817–16820 (1994).
[33]G. Mak and W. W. Rühle, "Femtosecond carrier dynamics in Ge measured by a luminescence up-conversion technique and near-band-edge infrared excitation," Phys. Rev. B **52**, R11584–R11587 (1995).
[34]T. Liu, L. Wang, G. Zhu, X. Hu, Z. Dong, Z. Zhong, Q. Jia, X. Yang, and Z. Jiang, "Dislocation-related photoluminescence of GeSn films grown on Ge (001) substrates by molecular beam epitaxy," Semicond. Sci. Technol. **33**, 125022 (2018).
[35]S. V. Kondratenko, S. S. Derenko, Y. I. Mazur, H. Stanchu, A. V. Kuchuk, V. S. Lysenko, P. M. Lytvyn, S.-Q. Yu, and G. J. Salamo, "Impact of defects on photoexcited carrier relaxation dynamics in GeSn thin films," J. Phys.: Condens. Matter **33**, 065702 (2020).
[36]S. De Cesari, A. Balocchi, E. Vitiello, P. Jahandar, E. Grilli, T. Amand, X. Marie, M. Myronov, and F. Pezzoli, "Spin-coherent dynamics and carrier lifetime in strained $Ge_{1-x}Sn_x$ semiconductors on silicon," Phys. Rev. B **99**, 035202 (2019).
[37]J. Menéndez, C. D. Poweleit, and S. E. Tilton, "Temperature-dependent photoluminescence in Ge: Experiment and theory," Phys. Rev. B **101**, 195204 (2020).
[38]L. Jiang, J. D. Gallagher, C. L. Senaratne, T. Aoki, J. Mathews, J. Kouvetakis, and J. Menéndez, "Compositional dependence of the direct and indirect band gaps in $Ge_{1-y}Sn_y$ alloys from room temperature photoluminescence: Implications for the indirect to direct gap crossover in intrinsic and n-type materials," Semicond. Sci. Technol. **29**, 115028 (2014).
[39]S. Al-Kabi, S. A. Ghetmiri, J. Margetis, W. Du, A. Mosleh, M. Alher, W. Dou, J. M. Grant, G. Sun, R. A. Soref, J. Tolle, B. Li, M. Mortazavi, H. A. Naseem, and S.-Q. Yu, "Optical characterization of Si-based $Ge_{1-x}Sn_x$ alloys with Sn compositions up to 12%," J. Electron. Mater. **45**, 2133–2141 (2016).
[40]V. Reboud, A. Gassenq, N. Pauc, J. Aubin, L. Milord, Q. M. Thai, M. Bertrand, K. Guilloy, D. Rouchon, J. Rothman, T. Zabel, F. Armand Pilon, H. Sigg, A. Chelnokov, J. M. Hartmann, and V. Calvo, "Optically pumped GeSn micro-disks with 16% Sn lasing at 3.1 μm up to 180 K," Appl. Phys. Lett. **111**, 092101 (2017).
[41]J. Menéndez, P. Wallace, C. Xu, C. Senaratne, J. Gallagher, and J. Kouvetakis, "Materials physics of GeSn-based semiconductor lasers," Mater. Today: Proc. **14**, 38–42 (2019). xXIII Latin American Symposium on Solid State Physics (SLAFES XXIII), San Carlos de Bariloche, Argentina, 10-13 April 2018.
[42]D. Rainko, Z. Ikonic, A. Elbaz, N. von den Driesch, D. Stange, E. Herth, P. Boucaud, M. El Kurdi, D. Grützmacher, and D. Buca, "Impact of tensile strain on low Sn content GeSn lasing," Sci. Rep. **9**, 259 (2019).
[43]O. Concepción, A. J. Devaiya, M. H. Zoellner, M. A. Schubert, F. Bärwolf, L. Seidel, V. Reboud, A. T. Tiedemann, J. Bae, A. Tchelnokov, Q. Zhao, C. A. Broderick, M. Oehme, G. Capellini, D. Grützmacher, and D. Buca, "Adaptive epitaxy of C-Si-Ge-Sn: Customizable bulk and quantum structures," Adv. Mater. 2506919 (2025).